Wu et al. *Zool. Res.* 2026, 47(3): 635−648
https://doi.org/10.24272/j.issn.2095-8137.2025.675
https://cstr.cn/32248.14.zr.2025.675

ZR Zoological Research

Article Open Access

Fatty acid synthase promotes Hantaan virus infection through lipogenic regulation in the tree shrew model

Yue-Chun Wu[1,2,3,#], Han-Song Qi[1,2,#], Feng-Yi Li[1,2,3], Jin-Xuan Yang[1,2,3], Ling Xu[1,3,4], Xiao-Qin Guo[1,2], Gui-Jun Chen[1,2], Ju-Min Zhou[1,2], Yong-Gang Yao[1,3,4,5], Xing-Lou Yang[1,2,3,5,*]

[1] *State Key Laboratory of Genetic Evolution* & *Animal Models*, *Kunming Institute of Zoology*, *Chinese Academy of Sciences*, *Kunming*, *Yunnan* 650201, *China*

[2] *Yunnan International Joint Laboratory of Zoonotic Viruses*, *Yunnan Key Laboratory of Biodiversity Information*, *Kunming Institute of Zoology*, *Chinese Academy of Sciences*, *Kunming*, *Yunnan* 650201, *China*

[3] *Kunming College of Life Science*, *University of Chinese Academy of Sciences*, *Kunming*, *Yunnan* 650204, *China*

[4] *Yunnan Key Laboratory of Animal Models and Human Disease Mechanisms*, *Yunnan Engineering Center on Brain Disease Models*, *Kunming Institute of Zoology*, *Chinese Academy of Sciences*, *Kunming*, *Yunnan* 650204, *China*

[5] *National Research Facility for Phenotypic* & *Genetic Analysis of Model Animals (Primate Facility)*, *National Resource Center for Non-Human Primates*, *and Kunming National High-Level Biosafety Research Center for Non-Human Primates*, *Kunming Institute of Zoology*, *Chinese Academy of Sciences*, *Kunming*, *Yunnan* 650107, *China*

ABSTRACT

Hantaan virus (HTNV) is the principal etiological agent of hemorrhagic fever with renal syndrome (HFRS) in Asia. To date, however, progress in defining mechanisms of host-pathogen interaction has been limited by the absence of an appropriate animal model. In the present study, the tree shrew (*Tupaia belangeri*) was shown to be permissive to HTNV infection and to recapitulate key renal pathology and immunological features observed in patients with HFRS. Following intranasal challenge, viral replication occurred predominantly in the kidney, spleen, and lung, accompanied by tubular dilation, glomerular congestion, and interstitial inflammation. Transcriptomic profiling further demonstrated that HTNV infection induced metabolic reprogramming to enhance fatty acid oxidation and suppress *de novo* lipogenesis. At the same time, fatty acid synthase (FASN), a key enzyme in lipid biosynthesis, proved to be indispensable for efficient viral replication. Notably, both FASN knockdown and pharmacological inhibition with TVB-3664 markedly suppressed HTNV proliferation through disruption of lipid droplet formation and subsequent amplification of type I interferon responses. Mechanistically, the HTNV nucleocapsid protein (NP) recruited and interacted with FASN, thereby modulating lipogenic activity and suggesting that HTNV exploits fatty acid metabolic pathways to support viral replication through NP-FASN interaction. Collectively, these findings establish a previously unrecognized link between HTNV replication and host lipid metabolic remodeling, identify FASN as a critical host determinant during infection, and highlight the FASN-dependent lipogenic pathway as a promising therapeutic target for HFRS.

Keywords: Hantaan virus; Tree shrews; Animal model; Fatty acid synthase; Virus-host interaction

INTRODUCTION

Hemorrhagic fever with renal syndrome (HFRS) remains a major zoonotic burden in East Asia, with Hantaan virus (HTNV), the prototype species of the genus *Orthohantavirus* in the family *Hantaviridae*, serving as the predominant etiological agent (Sehgal et al., 2023; Vaheri et al., 2013). Infection is acquired primarily through inhalation of aerosols contaminated with excreta from infected rodents and can progress to a severe clinical syndrome marked by vascular leakage, thrombocytopenia, and acute renal dysfunction. Given the substantial epidemic potential and public health threat associated with this virus, HTNV has been designated by the World Health Organization (WHO) as a priority pathogen (WHO, 2024). Despite extensive surveillance and vaccination efforts in endemic regions, therapeutic options remain limited, and no specific antiviral agent has entered routine clinical use. Progress toward a mechanistic understanding of HFRS pathogenesis has also been slowed by the lack of a susceptible experimental animal model that recapitulates the

---

Received: 12 April 2026; Accepted: 18 May 2026; Online: 19 May 2026

Foundation items: This work was supported by the National Natural Science Foundation of China (U2202216), Yunnan Province (202501CF070270, 202301AS070068, 202305AH340006, XDYC-QNRC-2022-0769), and Chinese Academy of Sciences (Y2023091, xbzg-zdsys-202302)

[#] Authors contributed equally to this work

[*] Corresponding author, E-mail: yangxinglou@mail.kiz.ac.cn

defining clinical and pathological features of human disease with sufficient fidelity. Common laboratory rodents such as mice and rats (McKee et al., 1985; Yamanouchi et al., 1984; Yoshimatsu et al., 1997) show restricted susceptibility to HTNV infection and fail to adequately reflect the spectrum of disease observed in humans, emphasizing the need for alternative animal systems with greater translational relevance.

The tree shrew (*Tupaia belangeri*) has emerged as a promising candidate to address this gap. This small mammal is phylogenetically more closely related to primates than to rodents (Yao et al., 2024; Ye et al., 2021), and increasing evidence has supported its utility in the study of multiple viral infections, including hepatitis viruses (Feng et al., 2017; Yang et al., 2015; Yu et al., 2026), influenza viruses (Sanada et al., 2019), and severe acute respiratory syndrome coronavirus 2 (SARS-CoV-2) (Xu et al., 2020; Zhao et al., 2020). Closer similarity of immune architecture and metabolic characteristics to those in humans further strengthens the value of this species as a biologically relevant experimental platform (Yao et al., 2024). These attributes establish the tree shrew as an attractive candidate model for defining hantavirus tropism, host responses, and disease mechanisms that drive HFRS.

Previous studies have indicated that HTNV pathogenicity is largely shaped by a dynamic interplay among viral replication, host immunity, and metabolic adaptation (Sehgal et al., 2023). To date, however, the molecular basis of these interactions remains elusive. Increasing evidence has established that viral replication and immune regulation are tightly linked to cellular metabolic state (Majdoul & Compton, 2022). In particular, many RNA viruses, including hepatitis C virus (HCV) (Huang et al., 2013; Vogt et al., 2013), dengue virus (DENV) (Tang et al., 2014; Wu et al., 2022), and SARS-CoV-2 (Dias et al., 2020), reprogram host lipid metabolism to sustain replication, promote virion assembly, and evade immune responses. A similar dependence has been documented in hantaviruses, in which host cholesterol metabolism is required at multiple stages of the infectious cycle, including viral entry through cholesterol-rich lipid raft microdomains that facilitate membrane fusion (Mittler et al., 2019). Consistent with this requirement, suppression of cholesterol biosynthesis through HMGCR-targeting statins such as atorvastatin or through CH25H-derived 25-hydroxycholesterol markedly inhibits HTNV replication by disrupting viral entry and restricting cholesterol availability (Dang et al., 2024). Further support has emerged from recent evidence showing that differences in tissue tropism and virulence between Old World and New World hantaviruses are closely associated with distinct patterns of host membrane utilization and metabolic dependence, particularly with respect to cholesterol-enriched membrane domains (Jeyachandran et al., 2025). Together, these observations identify cholesterol metabolism as a major host determinant of hantavirus infection and a promising target for host-directed antiviral intervention.

Despite these advances, however, current understanding remains narrowly centered on cholesterol metabolism, with other essential branches of lipid metabolism receiving far less attention. Among these, fatty acid biosynthesis is of particular interest because it provides essential substrates for membrane biogenesis, lipid modification, and virion production (Liu et al., 2021a; Tsui et al., 2025) . Fatty acid synthase (FASN), the core enzyme responsible for *de novo* lipogenesis, has emerged as a pivotal metabolic hub co-opted by a wide range of viruses to generate lipid substrates required for envelope formation and protein palmitoylation (Loperena González et al., 2025). Consistent with this role, pharmacological or genetic disruption of FASN has been shown to impair replication of multiple enveloped viruses (Liu et al., 2021b; Ohol et al., 2015), highlighting a broader requirement for lipogenic remodeling during viral infection. Nonetheless, whether HTNV similarly reprograms host lipid metabolism and specifically whether FASN-dependent lipogenic pathways contribute to efficient infection remain largely unresolved.

In this study, the tree shrew was established as a susceptible animal model for HTNV infection that recapitulated key pathological and immunological characteristics observed in patients with HFRS, thereby bridging the long-standing gap between conventional rodent models and human disease and enabling more physiologically relevant investigation of hantavirus-host interactions. Integrative transcriptomic and functional analyses further revealed a previously unrecognized contribution of host lipid metabolism to efficient HTNV replication and demonstrated that inhibition of FASN suppressed viral propagation while simultaneously enhancing innate antiviral responses. These findings expand current understanding of the metabolic requirements underlying hantavirus infection and highlight the dual role of FASN in promoting viral replication while modulating immune signaling.

MATERIALS AND METHODS

Biosafety and animal ethics

Animal experiments were performed in the Animal Biosafety Level 3 (ABSL-3) facility at the Kunming Institute of Zoology (KIZ), Chinese Academy of Sciences (CAS), whereas cell infection experiments were performed in the Biosafety Level 2 (BSL-2) facility of the same institute. All procedures involving animals were conducted in accordance with the Guidelines for the Care and Use of Laboratory Animals issued by the Ministry of Science and Technology of China. Furthermore, all experimental protocols were reviewed and approved by the Institutional Animal Care and Use Committee (IACUC) of KIZ, CAS (Approval No.: IACUC-TE-2024-04-002).

Cell lines

Vero E6 (ATCC: CRL-1587), HeLa (ATCC: CCL-2), HUVECs (ATCC: CRL-1730), A549 (ATCC: CCL-185), and HEK293T (ATCC: CRL-3216) cell lines were purchased from the National Collection of Authenticated Cell Cultures. Cells were cultured in Dulbecco's Modified Eagle Medium (DMEM, Thermo Fisher Scientific and Gibco, USA; Cat. No. C11995500BT) supplemented with 10% (v/v) fetal bovine serum (FBS) (Thermo Fisher Scientific and Gibco, USA; Cat. No. A5669701) at 37°C in a humidified incubator containing 5% CO_2.

Virus culture and titration

HTNV strain 76-118 was obtained from Wuhan University and propagated in suckling C57BL/6N mice. Brain tissue collected from inoculated mice was homogenized, centrifuged at 12 000 ×*g* for 10 min at 4°C, aliquoted, and stored at −80°C until use. Viral titers were determined in Vero E6 cells as described previously (Yang et al., 2025).

Animal susceptibility test

Tree shrews (5–6 years old) were obtained from the Animal Experimental Core Facility of KIZ, CAS. Infection was carried out through intraperitoneal and intranasal inoculation, with each experimental group comprising three males and three females. HTNV was administered at a dose of 1×10^6 $TCID_{50}$ per animal, whereas negative controls received physiological saline.

Animal infection model

A total of 32 tree shrews (16 males and 16 females) were assigned to HTNV infection and control groups, with four animals included in each group. Animals in the infection group received intranasal inoculation with HTNV at a dose of 1×10^6 $TCID_{50}$ per animal, whereas control animals were administered physiological saline. Body weight was recorded and rectal swabs were collected at 1, 3, 5, 7, and 15 days post-infection (dpi). At each designated time point, tree shrews were euthanized under approved ethical protocols. Heart, liver, spleen, lung, kidney, and intestinal tissues were then harvested. After tissue weights were recorded, samples were homogenized in DMEM to prepare tissue suspensions. Homogenates were centrifuged at 12 000 ×*g* for 10 min at 4°C, and supernatants were collected for viral RNA analysis. Viral RNA was isolated from tissue supernatants using a Nucleic Acid Extraction Kit (Vazyme, China) following the manufacturer's protocols. HTNV RNA levels were quantified by probe-based real-time quantitative polymerase chain reaction (RT-qPCR) using virus-specific primers and probes, and relative viral RNA levels were calculated based on Ct values after normalization to tissue weight. Primers and probes targeting the HTNV S gene were synthesized by Sangon Biotech: HTNV S forward 5'-ACATCTGAGGA GAAGCTACGG-3'; HTNV S reverse 5'-GGCAACCATG AAGAGCACAA-3'; and probe 5'-FAM-AGCATCATCGT CTATCTTACATCC-TAMRA-3'.

Hematological and serum biochemical analyses

At the indicated time points after HTNV infection, blood samples were collected via cardiac puncture. Approximately 1 mL of whole blood was used for complete blood count (CBC) analysis, and the remaining sample was allowed to clot for serum isolation prior to biochemical analysis.

Histopathological examination

Organ tissues collected from tree shrews were embedded in paraffin and sectioned at a thickness of 5 μm. Sections were mounted on glass slides and stained with hematoxylin and eosin (H&E). After staining, slides were sealed with neutral balsam and examined by light microscopy using a Digital Slide System VS120 (Olympus, Japan) to evaluate histopathological alterations.

Immunofluorescence assay

Infected cells and tissue sections were fixed and permeabilized for 15 min, followed by blocking with 5% bovine serum albumin (BSA, Sangon Biotech, China) prepared in phosphate-buffered saline (PBS, Servicebio, China) for 1 h. Samples were then incubated overnight at 4°C with a homemade rabbit anti-HTNV nucleocapsid protein (NP) antibody diluted in PBS containing 1% BSA. After washing, samples were incubated at room temperature for 2 h with either Alexa Fluor 488-conjugated goat anti-rabbit IgG (H+L) (Thermo Fisher Scientific, USA) or cyanine 3 (CY3)-conjugated secondary antibody (Thermo Fisher Scientific, USA). Following washing, nuclei were counterstained with 4',6-diamidino-2-phenylindole (DAPI; Abcam, UK) for 10 min. Images were captured and analyzed using an Axiovert 5 microscope (ZEISS, Germany).

RNA sequencing (RNA-seq)

Kidney and lung samples collected under different conditions (control, dpi 3, and dpi 5) were subjected to bulk RNA-seq, separately. At each time point, three tree shrew tissue samples were randomly selected as biological replicates for RNA sequencing. Library extracts were sequenced on the Illumina X Plus platform (Biomarker Technologies, China). Raw reads were assessed for quality using FastQC v.0.12.1, and low-quality reads and adapter sequences were removed using Trimmomatic v.0.39 (Bolger et al., 2014). Filtered reads were then mapped to the tree shrew genome (Ye et al., 2021) using HISAT2 v.2.2.1 (Kim et al., 2019). Raw counts for reads mapped to coding genes were summarized with featureCounts v.2.0.6 (Liao et al., 2014) and differential expression analysis was performed with the R package edgeR v.4.2.1 (Robinson et al., 2010). Differentially expressed genes (DEGs) were defined by an adjusted P-value<0.05 and absolute log fold change> 2. Over-representation analysis (ORA) and gene set enrichment analysis (GSEA) were conducted using ClusterProfiler v.4.12.6 (Wu et al., 2021; Yu et al., 2012).

Plasmid construction

All plasmids used in this study were generated by *in vitro* homologous recombination using a ClonExpress II One Step Cloning Kit (Vazyme, China). The full-length coding sequence of HTNV NP carrying a C-terminal S-tag was inserted into the pCAGGS backbone. Coding sequences of HTNV Gn, NP, and NP truncation mutants carrying an N-terminal Flag tag were inserted into the pCS2 backbone. Full-length HTNV NP carrying a C-terminal Flag tag was inserted into the pTomo backbone. The pCMV-FASN plasmid was purchased from Miaolin Biotechnology, China.

Oil Red O staining

At 48 h after HTNV infection, culture medium was removed and HeLa cells were washed twice with PBS. Cells were fixed in 4% paraformaldehyde at room temperature for 10 min and then washed twice with PBS. After a brief rinse in staining wash solution for 20 s, cells were incubated with Oil Red O solution (Beyotime, China) for 15 min at room temperature in the dark. Following staining, cells were rinsed with staining wash solution for 30 s, washed with PBS, and observed under an inverted microscope.

Cell viability assay and effect of inhibitors on HTNV replication

HeLa cells were seeded in 96-well plates and exposed to serial concentrations of the TVB-3664 inhibitor (MCE: S8563, USA) for 48 h. Cell viability was then evaluated using the Cell Counting Kit-8 (CCK-8, Beyotime, China) according to the manufacturer's instructions. To define the effects of inhibitor treatment on different stages of the HTNV replication cycle, HeLa cells were treated with TVB-3664 at designated time points, including 1 h and 12 h before infection and 1 h and 12 h post-infection. Cells were subsequently infected with HTNV at a multiplicity of infection (MOI) of 0.5 and incubated at 37°C in 5% CO_2 for 48 h. Total cellular RNA was then extracted for RT-qPCR analysis.

Triglyceride (TG) assay

Cellular TG levels were measured using a Triglyceride Assay Kit (Shanghai Youxuan, China). Briefly, HeLa cells cultured in 6-well plates were washed three times with ice-cold PBS and lysed with 100 μL of lysis buffer at room temperature for 10 min. Lysates were heated at 70°C for 10 min and centrifuged at 2 000 ×*g* for 5 min at 4°C, after which the supernatants were collected. Samples were incubated with the working solution at 37°C for 15 min, and absorbance was measured at 570 nm using a SpectraMax Mini microplate reader (Molecular Devices, USA).

Construction of the shFASN cell line

Lentiviral particles for stable FASN knockdown were produced in HEK293T cells by co-transfection of Lenti-shFASN-puro, psPAX2, and pMD2.G plasmids using Lipofectamine 3000 (Invitrogen, USA) according to the manufacturer's protocols. Plasmids were mixed at a ratio of 3:2:1, with a total DNA input of 3 µg per well. At 6 h post-transfection, the medium was replaced with fresh DMEM containing 2% FBS, and cells were cultured for an additional 48 h. Culture supernatants containing lentiviral particles were collected and centrifuged at 300 ×*g* for 5 min at 4°C, with the clarified supernatants then used to infect HeLa cells and HEK293T cells at an MOI of 0.5. After 48 h of infection, puromycin selection was initiated to establish stable HeLa-shFASN cell lines. FASN-targeting shRNA sequences were synthesized by Sangon Biotech: shFASN-1, 5'-GTTTGATGCCTCCTTCTTCG-3'; shFASN-2, 5'-CAACTACGGCTTTGCCAATT-3'.

FASN overexpression in HeLa cells

HeLa cells were seeded in 6-well plates and transfected with a FASN expression plasmid using Lipofectamine 2000 (Invitrogen) when cell confluence reached approximately 70%–80%. After 8 h, the transfection medium was replaced with fresh complete medium, and cells were cultured for a further 48 h to ensure sufficient FASN protein expression. At 48 h post-transfection, HTNV was added at an MOI of 0.5 and allowed to adsorb for 2 h at 37°C. The viral inoculum was removed, and cells were washed twice with PBS, followed by the addition of fresh complete medium for continued culture. Cells and culture supernatants were collected at 48 hpi. Viral replication was evaluated by viral RNA quantification and immunofluorescence assay targeting NP.

Detection of cRNA and vRNA

Selective detection of HTNV positive-strand and negative-strand RNA was performed using strand-specific reverse transcription followed by qPCR. Strand-specific reverse transcription reactions were carried out using gene-specific reverse or forward primers to selectively synthesize cDNA from positive- or negative-strand RNA, respectively: HTNV NP+, 5'-acatcaatcaagctctgtgcca-3'; HTNV NP−, 5'-aagatattgagtcaccatcatc-3'. Reactions lacking reverse transcriptase were included as negative controls to exclude nonspecific amplification and false-positive signals. The resulting cDNA was subsequently quantified by qPCR, and each sample was analyzed with at least three technical replicates.

Western blotting

HeLa cells were washed three times with ice-cold PBS and lysed with cold lysis buffer for 30 min. Lysates were clarified by centrifugation at 12 000 ×*g* for 10 min. Protein samples were separated by sodium dodecyl sulfate-polyacrylamide gel electrophoresis (SDS-PAGE), transferred to polyvinylidene fluoride (PVDF, Merck, Germany) membranes, and detected using specific primary antibodies followed by appropriate secondary antibodies. GAPDH was used as a loading control.

Co-immunoprecipitation (Co-IP)

HEK293T cells were transfected with plasmid pTomo-HTNV S-ORF-Flag-P2A-HygR to overexpress Flag-tagged HTNV N protein for 48 h. Cells were washed three times with ice-cold PBS and lysed in RIPA buffer (MCE, USA) at 4°C for 30 min. Lysates were centrifuged at 12 000×*g* for 10 min at 4°C, and supernatants were collected. In parallel, 2 µg of FASN-specific antibody (Abcam) was incubated with Protein A/G magnetic beads (MCE, USA) in PBS containing 0.5% Tween-20 (PBST) at 4°C for 2 h. Beads were washed three times with PBST binding buffer and incubated with cell lysates overnight at 4°C. Immunoprecipitated proteins were washed three times with PBST and eluted by boiling in sample buffer diluted with PBS for 10 min. Eluted proteins were analyzed by western blotting.

Statistical analysis

Statistical analysis was performed to evaluate differences between experimental groups. Data are presented as mean±standard error of the mean (SEM) or mean±standard deviation (SD), as indicated. Statistical significance between groups was determined using Student's *t*-test or one-way analysis of variance (ANOVA), as appropriate.

RESULTS

HTNV infection and tissue tropism in tree shrews

To better simulate the natural route of viral infection, six tree shrews were challenged with HTNV by either intraperitoneal or intranasal inoculation to assess susceptibility to infection. At 7 dpi, heart, liver, spleen, lung, kidney, and intestinal tissues were collected for virological analysis. Viral RNA and protein were detected in lung tissue from the intranasally infected group, whereas no evidence of infection was observed in the intraperitoneally infected group (Supplementary Figure S1A). Based on this result, subsequent experiments were performed using intranasal inoculation in 32 tree shrews (Figure 1A). Daily monitoring showed no significant changes in body weight or body temperature after infection (Figure 1B, C). To define viral kinetics and tissue distribution, serum and major organs were collected at 1, 3, 5, 7, and 15 dpi for viral RNA quantification. Viral RNA was detected in serum only at 7 dpi and only in a subset of animals (2/20) (Figure 1D). In contrast, tissue-associated viral RNA was identified in lung and kidney samples at 3 dpi and 5 dpi (Figure 1E, F), and in spleen tissue at 5 dpi and 7 dpi (Figure 1G). Viral loads ranged from 5.1×10^9 to 1.5×10^{11} copies/g, with the highest burden observed in the spleen. To determine viral infectivity in HTNV-positive samples, tissue homogenates were inoculated onto Vero E6 cells for viral titration. Replication-competent virus was recovered from the spleen, lung, and kidney, with titers of 158 $TCID_{50}$/g, 325 $TCID_{50}$/g, and 158 $TCID_{50}$/g, respectively, demonstrating productive infection in these organs (Figure 1H). The presence of HTNV NP in lung and kidney was further confirmed by immunofluorescence at 5 dpi (Figure 1I). Collectively, these results demonstrate that HTNV can successfully infect tree shrews and replicate in lung, spleen, and kidney tissues, accompanied by transient viremia.

Routine hematological and biochemical analysis of HTNV-infected tree shrews

Thrombocytopenia represents a hallmark clinical manifestation in infections caused by hemorrhagic fever viruses (Khaiboullina et al., 2005; Terajima & Ennis, 2011). To evaluate systemic responses to infection in the tree shrew model, whole blood samples were collected from HTNV-infected tree shrews for hematological examination. HTNV infection induced marked alterations in hematological

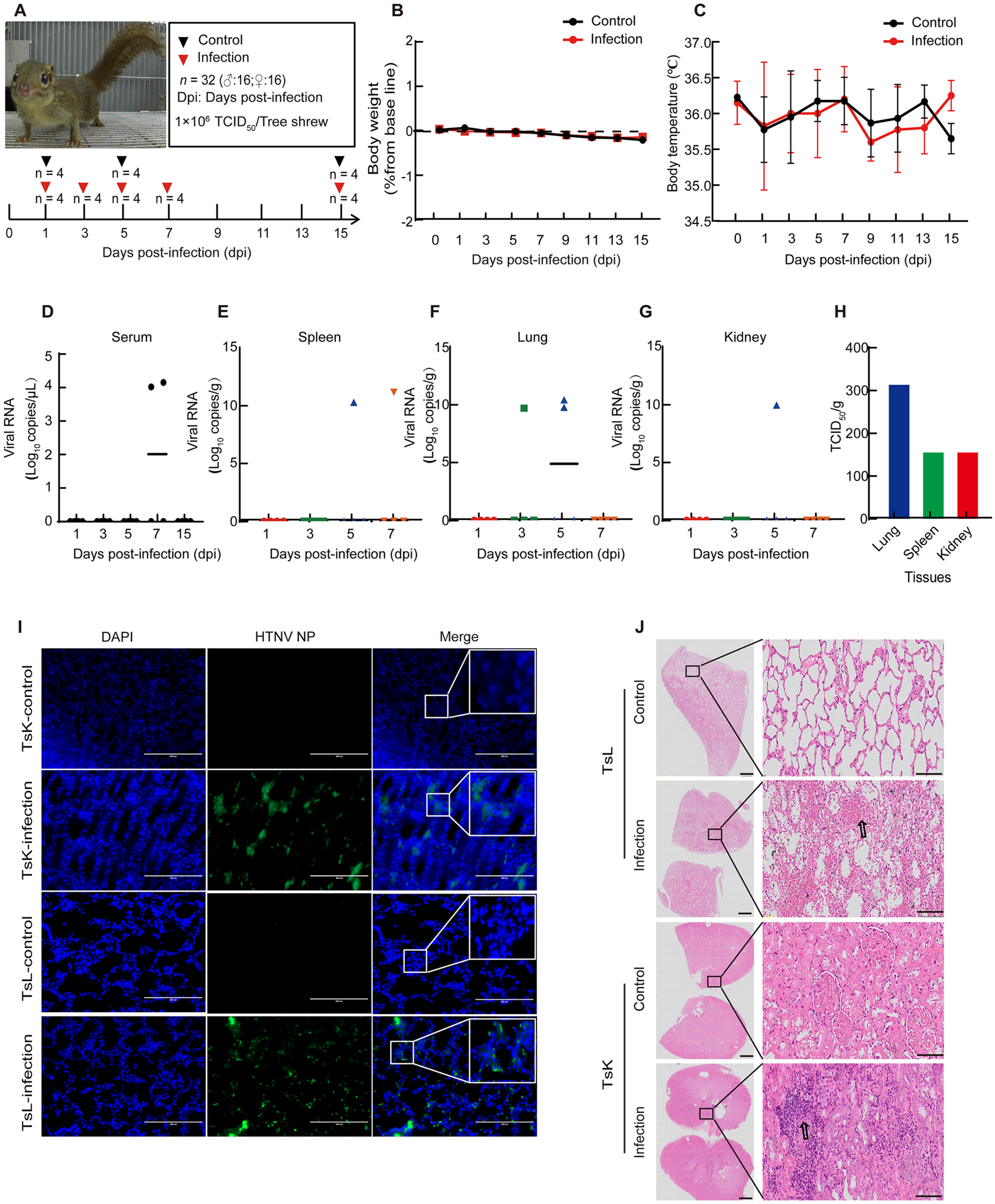

Figure 1 HTNV infects tree shrews and induces tissue damage

A: Schematic overview of the experimental design for HTNV infection in tree shrews (*n*=32). Tree shrews were inoculated intranasally with 1×10^6 $TCID_{50}$ of HTNV, while controls received an equal volume of physiological saline. Samples were collected at 1, 3, 5, 7, and 15 dpi. B: Changes in body weight in HTNV-infected (Infection) and mock-treated (Control) tree shrews. Data are presented as mean±SEM. C: Changes in body temperature in HTNV-infected tree shrews. D–G: Viral loads measured by RT-qPCR in serum (D), spleen (E), lung (F), and kidney (G) of HTNV-infected tree shrews. Each symbol represents one animal. Colors indicate different time points: red circles, 1 dpi (*n*=8); green squares, 3 dpi (*n*=4); blue triangles, 5 dpi (*n*=8); orange triangles, 7 dpi (*n*=4). Mock group, *n*=6. Each group contained equal numbers of males and females. H: Viral titration in HTNV-positive tree shrew tissues. One HTNV-positive sample each from lung, spleen, and kidney was selected. Tissue homogenates were serially diluted and used to infect Vero E6 cells. Viral titers were determined at 5 dpi, and $TCID_{50}$ values were calculated using the Reed-Muench method. I: Immunofluorescence of lung and kidney tissues from HTNV-infected tree shrews. Blue indicates DAPI-stained nuclei, and green represents HTNV viral protein. Scale bar: 200 μm. J: Histopathological changes in spleen, lung, and kidney tissues at different time points post-infection. Black arrows indicate areas with inflammatory cell infiltration. Scale bar: 1 mm in the left panel and 100 μm in magnified views of boxed areas on the right. TsL: Tree shrew lung tissue; TsS: Tree shrew spleen tissue; TsK: Tree shrew kidney tissue.

parameters, characterized by increased leukocyte and neutrophil counts accompanied by a pronounced reduction in lymphocyte numbers (Table 1). Biochemical profiling further revealed significant changes in several serum indicators, including albumin (ALB), aspartate aminotransferase (AST), globulin (GLOB), and total protein (TP), when compared with controls. Reduced ALB levels suggest possible impairment of glomerular filtration or hepatic function, whereas elevated AST levels indicate potential tissue injury associated with systemic inflammation and renal involvement (Table 2). Overall, these hematological and biochemical alterations indicate that HTNV infection in tree shrews recapitulates major clinical features reported in human HFRS cases (Vaheri et al., 2013).

Histopathological alterations in HTNV-infected tree shrews

Renal injury is a defining clinical feature of HFRS, with acute tubulointerstitial nephritis and inflammatory cell infiltration among the most frequent pathological manifestations (Reddy et al., 2023; Terajima & Ennis, 2011). Histopathological evaluation by H&E staining revealed that HTNV infection induced prominent tissue injury in tree shrews. In the kidney, pathological changes included glomerular congestion, degenerative swelling of tubular epithelium, perivascular inflammatory cell infiltration, marked cystic dilatation of renal tubules, and focal calcification. Lung tissue also exhibited evident pathological injury, including alveolar septal thickening, moderate inflammatory cell infiltration, and mild inflammatory infiltration in perivascular and peribronchial regions. In the spleen, lesions were predominantly characterized by shrinkage and atrophy of lymphoid nodules together with a reduced number of lymphoid follicles (Figure 1J).

HTNV infection triggers host immune responses and lipid metabolism reprogramming in tree shrews

Aberrant inflammatory cytokine production is a well-recognized feature of HFRS and contributes substantially to disease pathogenesis (Vaheri et al., 2013). To examine inflammatory responses in the tree shrew model, expression of representative cytokines was quantified in kidney tissue by RT-qPCR. Interleukin-6 (*IL-6*) expression increased after infection and reached a maximum at 7 dpi. Tumor necrosis factor α (*TNF-α*) and *IL-1β* also showed moderate elevation at 7 dpi, whereas *IL-8* displayed a pronounced increase at 3 dpi (Supplementary Figure S2B, G). In contrast, no significant change was detected for interferon γ (*IFN-γ*). To further define the molecular mechanisms associated with HTNV-induced tissue injury and host responses, transcriptomic profiling was performed in kidney and lung tissues collected at 3 dpi and 5 dpi, with uninfected animals used as controls and three biological replicates included for each time point. Principal component analysis (PCA) of the transcriptomic data revealed clear separation of infected and control samples at 3 dpi (Figure 2A; Supplementary Figure S1). Differential expression analysis conducted separately in kidney and lung identified broad transcriptional remodeling after infection, with extensive changes already evident at 3 dpi in both tissues (Figure 2B). GSEA further demonstrated widespread enrichment of pathways related predominantly to immune regulation and inflammatory responses across infected groups (Figure 2C, D). Although specific enriched signatures differed between tissues and time points, 17 shared gene sets were consistently linked to immune-associated processes (Figure 2E, F). These transcriptomic patterns broadly align with the RT-qPCR results, which showed increased expression of immune-response markers, including *IFN-γ*, *TNF-α*, *IL-6*, and *IL-1β* (Supplementary Figure S2B, G).

Table 1 Blood routine test results of tree shrews from different experimental groups

Parameter	Before HTNV inoculation	After HTNV inoculation						
		Total	*P*-value	1 dpi	3 dpi	5 dpi	7 dpi	15 dpi
White blood cell count (×10^9/L)	14.70±4.10	59.59±22.48	0.022	61.35±37.12	81.85±8.41	55.95±1.91	38.20±6.36	60.60±33.38
Lymphocyte count (×10^9/L)	9.10±3.96	0.29±0.21	0.011	0.30±0.28	0.45±0.21	0.25±0.07	0.10±0	0.35±0.35
Monocyte count (×10^9/L)	0.70±0.14	0.79±0.47	0.8132	0.85±0.78	1.25±0.21	0.70±0	0.35±0.07	0.80±0.71
Neutrophils count (×10^9/L)	4.90±0.28	58.51±21.81	0.022	60.20±36.06	80.15±7.99	55.00±1.84	37.75±6.29	59.45±32.31
Lymphocyte percentage (%)	60.60±9.76	0.42±0.19	0.022	0.40±0.28	0.60±0.14	0.30±0.14	0.30±0	0.50±0.28
Monocyte percentage (%)	5.00±2.40	1.19±0.33	0.011	1.20±0.57	1.50±0.14	1.20±0	0.90±0.14	1.15±0.49
Granulocyte percentage (%)	34.40±7.35	98.36±0.50	0.011	98.40±0.85	97.90±0.28	98.35±0.07	98.80±0.14	98.35±0.78

Data are presented as mean±SD. *P*-values indicate differences before and after inoculation (total: mean across all time points), determined using unpaired Student's *t*-test, with $P<0.05$ considered statistically significant.

Table 2 Blood biochemical analysis results of tree shrews from different experimental groups

Parameter	Before HTNV inoculation	After HTNV inoculation						
		Total	*P*-value	1 dpi	3 dpi	5 dpi	7 dpi	15 dpi
ALB	3.07±0.49	1.94±0.71	0.0353	2.17±1.25	1.15±0.07	1.83±0.32	2.23±0.834	2.07±0.25
ALT	47.67±7.57	67.21±29.92	0.2536	68.00±24.76	45±18.38	55.67±15.63	88.33±50.65	55±1.41
GLOB	2.83±0.38	2.13±0.41	0.0768	2.27±0.47	1.6±0.14	2.03±0.38	2.30±0.44	2.40±0.28
TP	5.87±0.47	4.11±1.07	0.0161	4.47±1.70	2.80±0.28	3.87±0.60	4.53±1.24	4.45±0.64
(ALB/GLOB)	1.10±0.30	0.90±0.19	0.2357	0.93±0.32	0.75±0.07	0.93±0.21	1.00±0.20	0.85±0.07
AST	17.33±12.10	28.07±15.39	0.1786	48.33±10.97	25.00±4.24	17.67±3.06	31.33±20.26	18.00±1.41
BUN	27.67±6.43	51.50±42.09	0.7268	64.67±56.58	86.00±62.23	27.00±10.58	32.00±37.64	36.5±23.33
CHOL	92.00±21.63	70.57±19.36	0.1411	65.67±21.55	43.50±0.71	63.00±12.17	82.67±12.50	94.00±4.24

Data are presented as mean±SD. *P*-values indicate differences before and after inoculation (total: mean across all time points), determined using unpaired Student's *t*-test, with $P<0.05$ considered statistically significant. BUN: Blood urea nitrogen; TP: Total protein; ALB: Albumin; ALT: Alanine aminotransferase; AST: Aspartate aminotransferase; GLOB: Globulin; CHOL: Cholesterol.

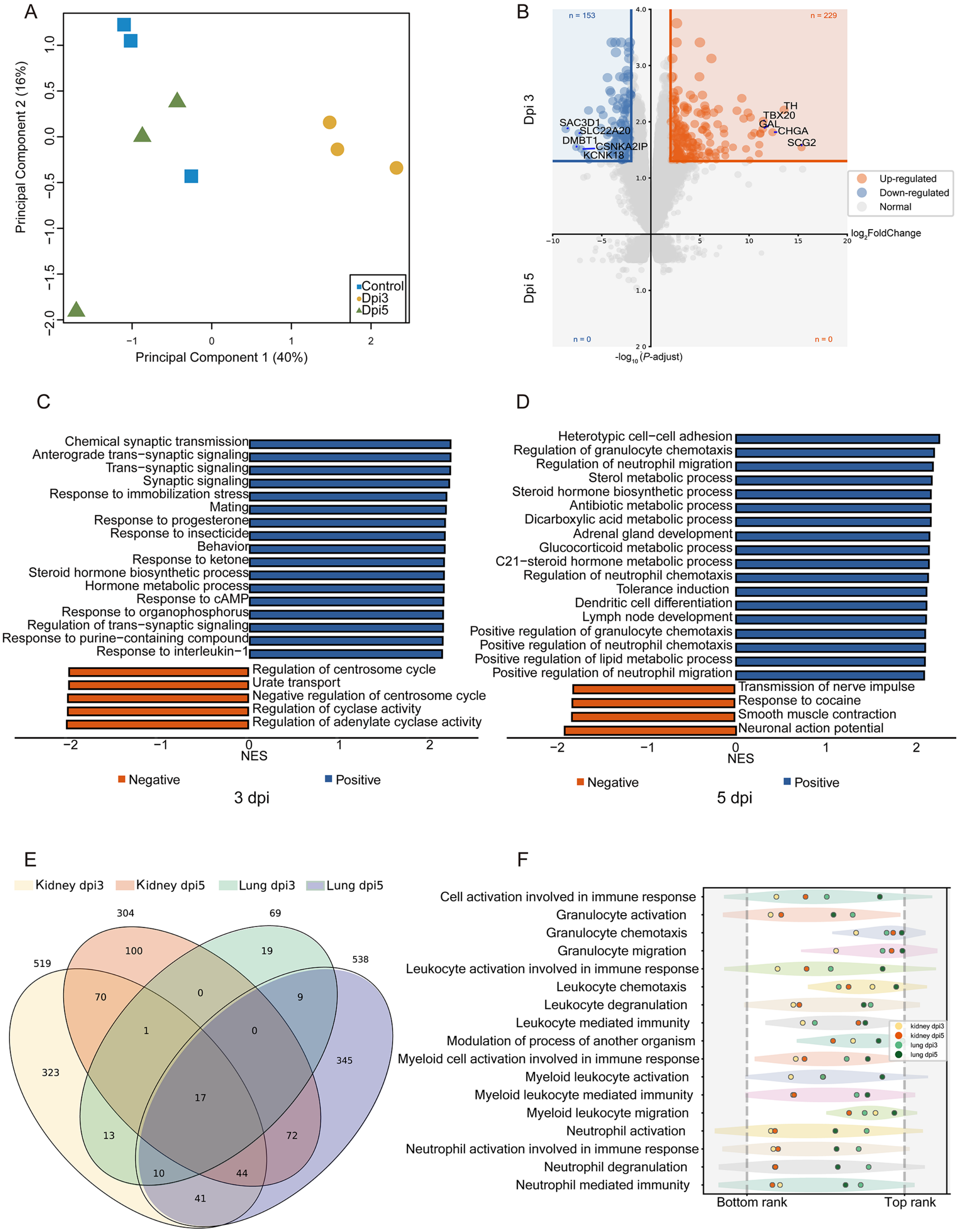

Figure 2 Transcriptional profiling of immune-related genes in kidneys from HTNV-infected tree shrews

A: Principal component analysis (PCA) of transcriptional profiles in kidney tissues from HTNV-infected tree shrews at 3 dpi (*n*=3) and 5 dpi (*n*=3), together with uninfected (*n*=3) controls. B: Volcano plots showing differentially expressed genes (DEGs) in kidney tissues at 3 dpi and 5 dpi. C, D: Bar plots showing normalized enrichment scores (NES) from gene set enrichment analysis (GSEA) of Gene Ontology (GO) biological process (BP) terms in kidney tissues of tree shrews at 3 dpi and 5 dpi. E: Venn diagram showing overlap among significantly enriched biological pathways identified by GSEA in kidney and lung tissues at 3 dpi and 5 dpi. F: Violin plot showing rank distribution of biological pathways shared among corresponding significantly enriched datasets.

Suppression of fatty acid synthesis restricts HTNV replication *in vitro*

Transcriptomic profiling revealed a pronounced metabolic remodeling response during HTNV infection, with strong induction of pathways related to fatty acid oxidation, lipid catabolism, and cholesterol metabolism, accompanied by relative suppression of fatty acid biosynthesis (Figure 3A). This pattern suggested that infection redirected host lipid metabolism away from anabolic lipid production toward catabolic programs to support the energetic and biosynthetic demands of viral propagation. To investigate the functional role of lipid metabolism in HTNV infection, transcriptomic and GSEA analyses indicated that in HTNV-infected tree shrew kidney tissues, pathways related to fatty acid oxidation and lipid catabolism were significantly upregulated (Figure 3A). As FASN is the central enzyme driving *de novo* lipogenesis (Menendez & Lupu, 2007; Wakil & Abu-Elheiga, 2009), disruption of this pathway was predicted to limit the lipid supply required for efficient HTNV replication and assembly. To test this possibility, HTNV permissiveness was first compared across A549 cells, HUVECs, and HeLa cells. Among these cell types, HeLa cells showed the highest susceptibility to infection and were therefore selected for subsequent *in vitro* experiments (Supplementary Figure S3A). Following HTNV infection, endogenous FASN expression in HeLa cells increased significantly at 48 hpi (Figure 3B), indicating that viral infection was accompanied by induction of the host lipogenic machinery during infection.

To define the functional relevance of FASN in this process, stable FASN-deficient HeLa cells were established, and knockdown efficiency was validated at both the transcript and protein levels by RT-qPCR and western blotting (Figure 3C, D). Infection of these cells with HTNV at an MOI of 0.5 showed that knockdown of FASN expression markedly impaired viral replication (Figure 3E). A comparable inhibitory effect was observed after treatment with the FASN inhibitor TVB-3664 (Figure 3F), further supporting a role for *de novo* fatty acid synthesis in efficient HTNV replication. To determine whether this FASN-dependent requirement extended to a kidney-derived cellular context, FASN was depleted in HEK293T cells, which are relevant to the renal tropism observed in the tree shrew model. FASN depletion consistently suppressed HTNV replication in HEK293T cells (Supplementary Figure S3B, C). Conversely, transient restoration of FASN expression in FASN-deficient HeLa cells increased HTNV RNA abundance following infection compared with FASN-deficient cells without re-expression (Figure 3G). Consistent with these findings, western blot analysis showed that FASN knockdown also reduced HTNV NP expression (Figure 3H).

Given that lipid synthesis is closely linked to intracellular TG storage and lipid droplet biogenesis, these parameters were further examined after infection. Results showed that HTNV challenge increased intracellular TG content and promoted lipid droplet accumulation in HeLa cells at 48 hpi compared with control cells (Figure 3I). In contrast, neither FASN-deficient cells nor cells exposed to the FASN inhibitor showed significant infection-associated increases in TG levels or lipid droplet abundance at the same time point relative to the corresponding controls (Figure 3J, K; Supplementary Figure S3D). In addition, exogenous TG supplementation further increased HTNV viral load, as determined by RT-qPCR (Figure 3L). Lipid droplet accumulation was also detected in HTNV-positive tree shrew tissues (Supplementary Figure S3G). Together, these results indicate that FASN-driven lipogenic activity supports efficient HTNV replication and that disruption of fatty acid synthesis restricts viral propagation *in vitro*.

FASN facilitates HTNV replication but is dispensable for viral entry

To determine the stage of the HTNV infectious cycle influenced by FASN, the effects of FASN depletion on viral entry were first examined. Knockdown of FASN did not impair viral attachment or internalization (Figure 4A, B), indicating that early entry events proceeded independently of this enzyme. The impact of FASN depletion on later stages of infection was then assessed by quantifying HTNV levels in both culture supernatants and cell lysates at 36 hpi. Reduced viral levels were detected in both compartments following FASN knockdown (Figure 4C; Supplementary Figure S3E), suggesting that stages downstream of viral entry were impaired. More notably, quantification of cRNA and vRNA showed that depletion of FASN significantly suppressed viral transcription and genome replication (Figure 4D, E), identifying replication as the principal stage affected by loss of FASN activity. A complementary pharmacological approach yielded a consistent pattern. Treatment with 50 μmol/L TVB-3664 for 2 h before infection or 2 h after infection did not significantly alter viral output (Supplementary Figure S3F), likely because this short exposure was insufficient to produce effective FASN inhibition. In contrast, 12 h of pre-treatment followed by continuous inhibitor exposure during infection produced a modest reduction in viral RNA levels (Figure 4F), further indicating that inhibition of FASN primarily impairs HTNV replication rather than viral entry.

FASN interacts with HTNV NP to facilitate viral replication

To further define the mechanism linking FASN to HTNV replication, the potential involvement of viral proteins in FASN-dependent regulation was examined. Because viral glycoproteins primarily function during viral entry, subsequent analyses focused on HTNV NP as a candidate mediator of post-entry events. Transient expression of HTNV NP in HeLa cells revealed clear spatial overlap between NP and FASN by confocal microscopy at 48 hpi (Figure 5A). This association was further substantiated by co-immunoprecipitation, which confirmed physical interaction between FASN and HTNV NP (Figure 5B). To determine whether this interaction alters host lipid metabolism, a stable HeLa cell line expressing HTNV NP was generated using lentiviral transduction (Figure 5C). Quantification of intracellular TG levels showed that stable NP expression increased TG levels relative to control cells (Figure 5D). Consistent with this result, Oil Red O and BODIPY staining demonstrated enhanced lipid droplet accumulation in NP-expressing HeLa cells (Figure 5E, F). These findings suggest that HTNV NP-FASN association promotes lipogenic remodeling and lipid droplet formation, supporting a role for this interaction in viral modulation of host lipid metabolism. Consistently, FASN showed extensive cytoplasmic colocalization with NP and formed aggregate-like structures. To define the NP regions involved in FASN recruitment, six NP truncation constructs were generated. Multiple NP regions contributed to FASN recruitment and aggregation, with the N-terminal region showing the strongest effect. These results indicate that NP-FASN interaction requires the structural context of intact NP rather than a single isolated domain (Supplementary Figure S3H, I).

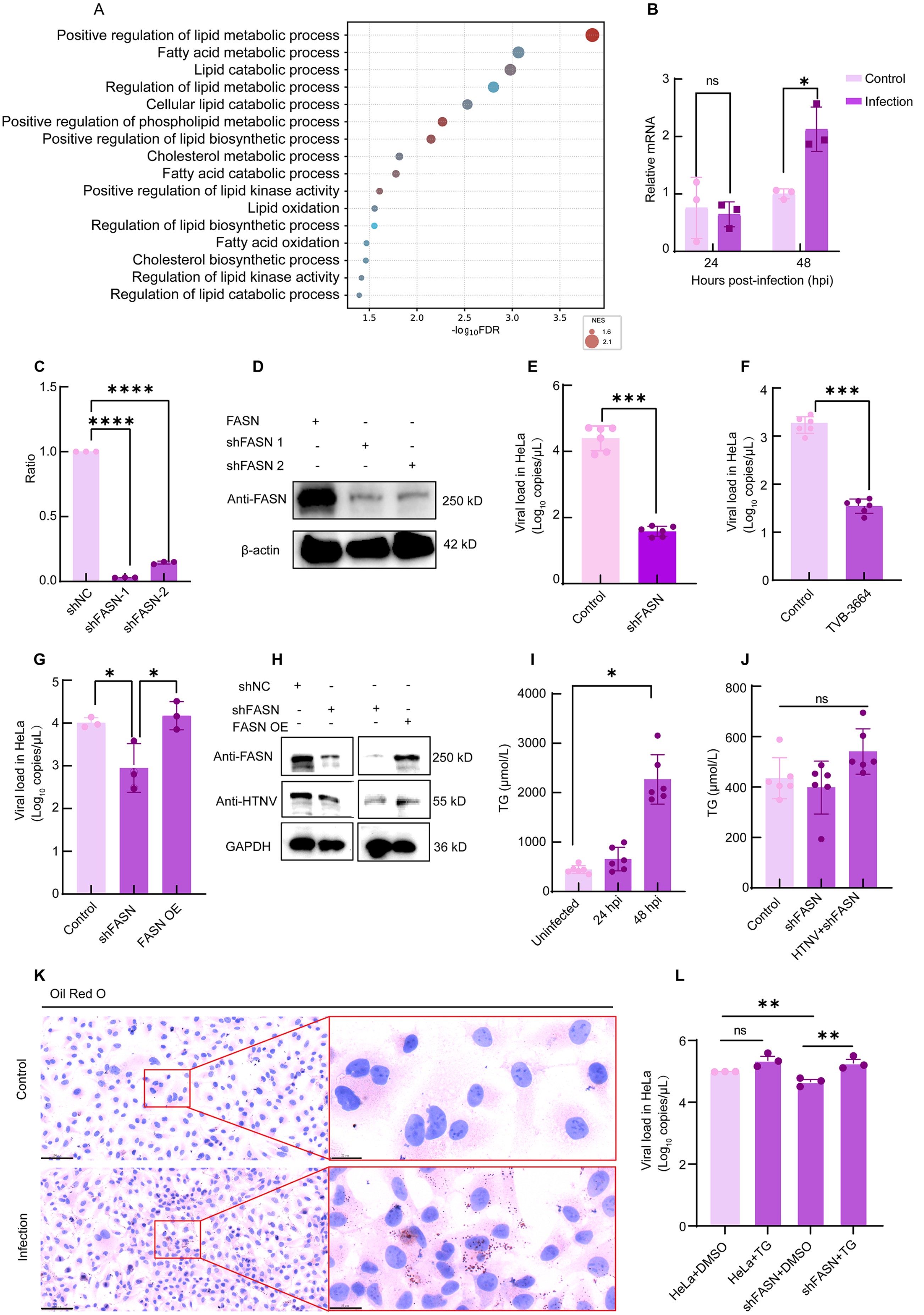
A
Positive regulation of lipid metabolic process
Fatty acid metabolic process
Lipid catabolic process
Regulation of lipid metabolic process
Cellular lipid catabolic process
Positive regulation of phospholipid metabolic process
Positive regulation of lipid biosynthetic process
Cholesterol metabolic process
Fatty acid catabolic process
Positive regulation of lipid kinase activity
Lipid oxidation
Regulation of lipid biosynthetic process
Fatty acid oxidation
Cholesterol biosynthetic process
Regulation of lipid kinase activity
Regulation of lipid catabolic process
1.5
2.0
2.5
3.0
3.5
-log10FDR
NES
1.6
2.1
B
Relative mRNA
0
1
2
3
ns
*
Control
Infection
24
48
Hours post-infection (hpi)
C
Ratio
0.0
0.5
1.0
1.5
****
****
shNC
shFASN-1
shFASN-2
D
FASN + - -
shFASN 1 - + -
shFASN 2 - - +
Anti-FASN
250 kD
β-actin
42 kD
E
Viral load in HeLa (Log10 copies/μL)
0
2
4
6
***
Control
shFASN
F
Viral load in HeLa (Log10 copies/μL)
0
1
2
3
4
***
Control
TVB-3664
G
Viral load in HeLa (Log10 copies/μL)
0
1
2
3
4
5
*
*
Control
shFASN
FASN OE
H
shNC + - - -
shFASN - + + -
FASN OE - - - +
Anti-FASN
250 kD
Anti-HTNV
55 kD
GAPDH
36 kD
I
TG (μmol/L)
0
1000
2000
3000
4000
*
Uninfected
24 hpi
48 hpi
J
TG (μmol/L)
0
200
400
600
800
ns
Control
shFASN
HTNV+shFASN
K
Oil Red O
Control
Infection
L
Viral load in HeLa (Log10 copies/μL)
0
2
4
6
**
ns
**
HeLa+DMSO
HeLa+TG
shFASN+DMSO
shFASN+TG

Figure 3 Suppression of fatty acid synthesis restricts HTNV replication

A: Normalized enrichment scores (NES) from gene set enrichment analysis (GSEA) performed with clusterProfiler. FDR, false discovery rate. B: Relative *FASN* mRNA expression in HeLa cells infected with HTNV at an MOI of 0.5 (Infection) or left uninfected (Control). Cells were harvested at 24 hpi and 48 hpi, and endogenous FASN expression was quantified. C, D: Relative FASN mRNA (C) and protein (D) levels in HeLa cells transduced with shFASN-1 or shFASN-2, with shNC used as the control. Cells were infected with lentiviruses carrying shFASN-1 or shFASN-2, harvested after 48 h, and analyzed by RT-qPCR (C) or western blotting (D). FASN protein was detected with mouse anti-FASN antibody, with β-actin used as an internal control. E: Effect of FASN knockdown on HTNV replication. Control HeLa cells and FASN-knockdown HeLa cells were infected with HTNV at an MOI of 0.5 for 48 h, and viral RNA levels in cell lysates were quantified by RT-qPCR. F: Effect of TVB-3664 on HTNV replication. HeLa cells were treated with or without TVB-3664 for 12 h, then infected with HTNV at an MOI of 0.5 for 48 h before sample collection. G: Viral load quantification in HTNV-infected HeLa cells overexpressing FASN (FASN OE). FASN was overexpressed in HeLa–FASN knockdown cells, followed by infection with HTNV at an MOI of 0.5. Viral RNA levels were measured by RT-qPCR at 48 h post-infection. H: Western blot analysis of HTNV NP expression following FASN knockdown (shFASN) or FASN overexpression (FASN OE). Control HeLa cells (shNC), HeLa-FASN knockdown cells, and FASN-overexpressing cells (FASN OE) were infected with HTNV at an MOI of 0.5 for 48 h. HTNV NP expression was analyzed by western blotting. FASN protein expression was detected using a mouse anti-FASN antibody, and GAPDH was used as an internal control. I: Intracellular triglyceride (TG) levels in HeLa cells after HTNV infection. HeLa cells were infected with HTNV at an MOI of 0.5, and TG content was measured at 24 hpi and 48 hpi. Uninfected cells served as controls. J: Effects of FASN knockdown on intracellular TG levels during HTNV infection. Control group consisted of knockdown cells without infection and infected normal cells. FASN knockdown cells were infected with HTNV at an MOI of 0.5, and TG content was measured at 48 hpi. Data are presented as mean±SD. ns: Not significant; ****: P<0.0001; ***: P<0.001; *: P<0.05; Statistical significance was determined using Student's *t*-test for B, E, and F, and one-way ANOVA for C, G, I, and J. K: Lipid droplet accumulation in HeLa cells after HTNV infection. HeLa cells were infected with HTNV at an MOI of 0.5, and lipid droplet content was detected by Oil Red O staining. Uninfected cells served as controls. Scale bar: 100 μm in the left panel and 25 μm in magnified views of boxed areas on the right. L: Viral RNA copy quantification in HTNV-infected HeLa cells supplemented with triglyceride (HeLa+TG). Triglyceride was supplemented into FASN-knockdown HeLa cells (shFASN+TG) and HeLa cells (HeLa+TG), followed by infection of HTNV at an MOI of 0.5. Viral RNA levels were quantified by RT-qPCR at 48 h post-infection. Control groups were set as follows: FASN-knockdown HeLa cells treated with DMSO (shFASN+DMSO) and HeLa cells treated with DMSO (HeLa+DMSO).

FASN inhibition enhances IFN-stimulated gene (ISG) expression

ISGs are central components of the host antiviral response (Wang et al., 2012). Given that lipid metabolic pathways are implicated in innate immunity, the effect of FASN inhibition on expression of innate immune genes, particularly ISGs, was further examined. Notably, both genetic depletion and pharmacological inhibition of FASN significantly increased IFN-α and IFN-β expression and strongly induced antiviral effectors such as *CXCL10* and *ISG15* (Supplementary Figure S4). These results suggest that disruption of FASN-dependent lipid metabolism impedes HTNV replication by strengthening IFN-I responses and antiviral factor production.

DISCUSSION

This study established the tree shrew as a valuable and susceptible small-animal model for HTNV infection and identified FASN-dependent lipogenesis as a key metabolic program that supports viral replication. Beyond recapitulating major pathological features of disease, this model provides an experimental framework for dissecting the metabolic mechanisms through which HTNV reshapes host biology to promote infection.

Although multiple animal systems have been used in hantavirus research (Jonsson et al., 2010), the tree shrew exhibited several integrated features that increase relevance to human HFRS. Histopathological assessment together with viral load profiling showed that HTNV localized predominantly to the kidney, spleen, and lung (Figure 1). Notably, renal injury was characterized by glomerular congestion, tubular dilation, and interstitial hemorrhage, closely resembling the renal pathology observed in patients with HFRS. Although conventional laboratory mice can support HTNV infection, viral distribution in these models is more commonly detected in organs such as the lung and liver and does not fully reflect the kidney-dominant disease pattern that defines human HFRS (Heaton & Randall, 2011; Vial et al., 2023). In contrast, HTNV infection in tree shrews was accompanied by clear renal pathological alterations, together with detectable viral protein in the kidney, a pattern that more closely parallels the course of viremia and renal injury observed in clinical disease (Vial et al., 2023). In line with previous observations in experimentally infected cynomolgus macaques (McElroy et al., 2002), uniformly high viral titers were not consistently achieved in this model. Nevertheless, the tree shrew reproduced clinically meaningful organ tropism and host responses that remain difficult to capture in conventional mouse models.

The biological relevance of this model may also derive from the similarity of immune-related pathways between tree shrews and humans. Comparative genomic and transcriptomic analyses have shown that this species shares more than 85% similarity with humans in immune-related genes, including IFN-I receptors, pattern recognition receptors, and key components of cytokine signaling networks (Li et al., 2012). These immunological characteristics provide a mechanistic explanation for the pronounced innate immune activation observed after HTNV infection in the present study, including induction of *IL-6, IL-1β*, and *IL-1RN*. Such cytokine dysregulation resembles inflammatory response patterns reported in HFRS patients (Guo et al., 2017), further supporting the value of the tree shrew for studying HTNV immunopathogenesis. At the same time, substantial genetic heterogeneity within this species, together with the lack of inbred lines, likely contributes to pronounced inter-individual variation, inconsistent infection outcomes, and relatively modest viral infection titers. Therefore, further refinement of experimental design and model standardization will be required to reduce biological variability and improve reproducibility.

Transcriptomic profiling of kidney tissues from HTNV-infected tree shrews revealed extensive remodeling of host metabolic and immune programs following infection (Figure 2). GSEA demonstrated that these infection-induced changes

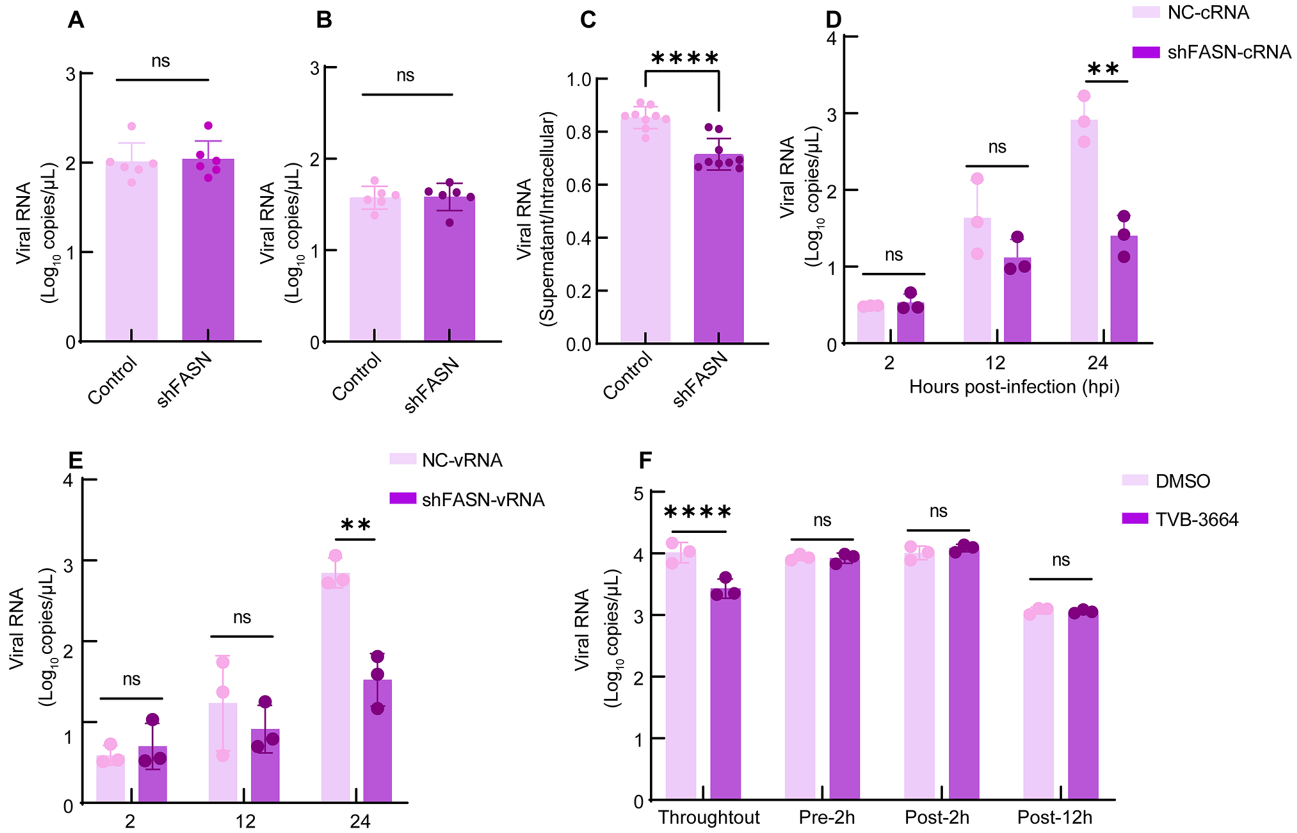

Figure 4 FASN depletion impairs HTNV replication but not viral entry

A,B: Effect of FASN knockdown on HTNV attachment (A) and internalization (B). HeLa-FASN knockdown (shFASN) cells were infected with HTNV at an MOI of 0.5 at 4°C for 1 h, then at 37°C for 2 h. RNA associated with internalized virus was quantified by RT-qPCR. C: Effect of FASN knockdown on HTNV release. Control HeLa cells and FASN-knockdown HeLa cells were infected with HTNV at an MOI of 0.5 for 36 h. Supernatants and cell lysates were collected separately, and viral RNA levels were quantified by RT-qPCR. Release efficiency was calculated as the ratio of viral RNA in the supernatant to that in the corresponding cell lysate. D, E: Effect of FASN knockdown on HTNV transcription and replication. FASN knockdown cells were infected with HTNV at an MOI of 0.5, and samples were collected at 2, 12, and 48 hpi. Strand-specific reverse transcription was performed using reverse or forward primers, followed by qPCR quantification of the resulting cDNA. F: Effect of TVB-3664 on HTNV replication in HeLa cells. HeLa cells were treated with TVB-3664 (50 μmol/L) at different time points during infection, and viral replication was quantified by RT-qPCR. Cells were exposed to TVB-3664 throughout the entire period, including a 12-h pretreatment period. Pre-2 h: Cells were treated with TVB-3664 for 2 h before infection; Post-2 h: Cells were treated with TVB-3664 for 2 h after infection; Post-12 h: Cells were treated with TVB-3664 for 12 h after infection. After each treatment, the medium was removed and replaced with 2% DMEM for 48 h before sample collection. Data are presented as mean±SD. ns: Not significant; ****: *P*<0.0001; **: *P*<0.01. Statistical significance was determined using Student's *t*-test.

were characterized by a broad shift in metabolic state, with strong enrichment of pathways involved in fatty acid oxidation, lipid degradation, and cholesterol metabolism, together with suppression of pathways associated with fatty acid biosynthesis (Figure 3A). Such coordinated reprogramming suggests that HTNV redirects host lipid homeostasis away from anabolic pathways toward catabolic processes to satisfy the energetic and structural demands of viral replication. Consistent with this interpretation, HTNV infection markedly increased endogenous FASN expression, whereas depletion of FASN significantly reduced viral RNA replication and NP expression, accompanied by decreased intracellular TG levels and lipid droplet accumulation (Figure 3). These findings expand current understanding beyond the previously recognized dependence of HTNV on cholesterol metabolism (Dang et al., 2024; Mittler et al., 2019) and identify *de novo* fatty acid synthesis as another important lipogenic pathway exploited during infection. This conclusion is consistent with previous studies showing that fatty acid metabolism is important for the replication of multiple RNA viruses, including HCV, SARS-CoV-2 and MERS-CoV (Heaton & Randall, 2011; Tanner & Alfieri, 2021; Yuan et al., 2019).

FASN showed clear colocalization with HTNV NP, and NP overexpression was sufficient to increase intracellular TG content and promote lipid droplet accumulation (Figure 5). Mapping analysis using six truncated NP variants showed that FASN redistribution was not driven by a single discrete NP segment. Instead, several regions contributed to FASN recruitment and cytoplasmic aggregation, with the N-terminal region exerting the strongest effect (Supplementary Figure S3H, I). Functional comparison of full-length NP and the truncation variants further showed that only intact NP produced a statistically significant alteration in cellular TG levels, although the N-terminal fragment also increased TG content (data not shown). These results indicate that efficient NP-FASN interaction and the associated lipogenic response require the broader structural configuration of intact NP. Furthermore, these observations reveal a direct connection between HTNV structural components and host lipogenic machinery, suggesting that HTNV reorganizes local lipid metabolism to support replication. FASN-derived palmitate may provide one mechanistic link, as palmitate serves as a

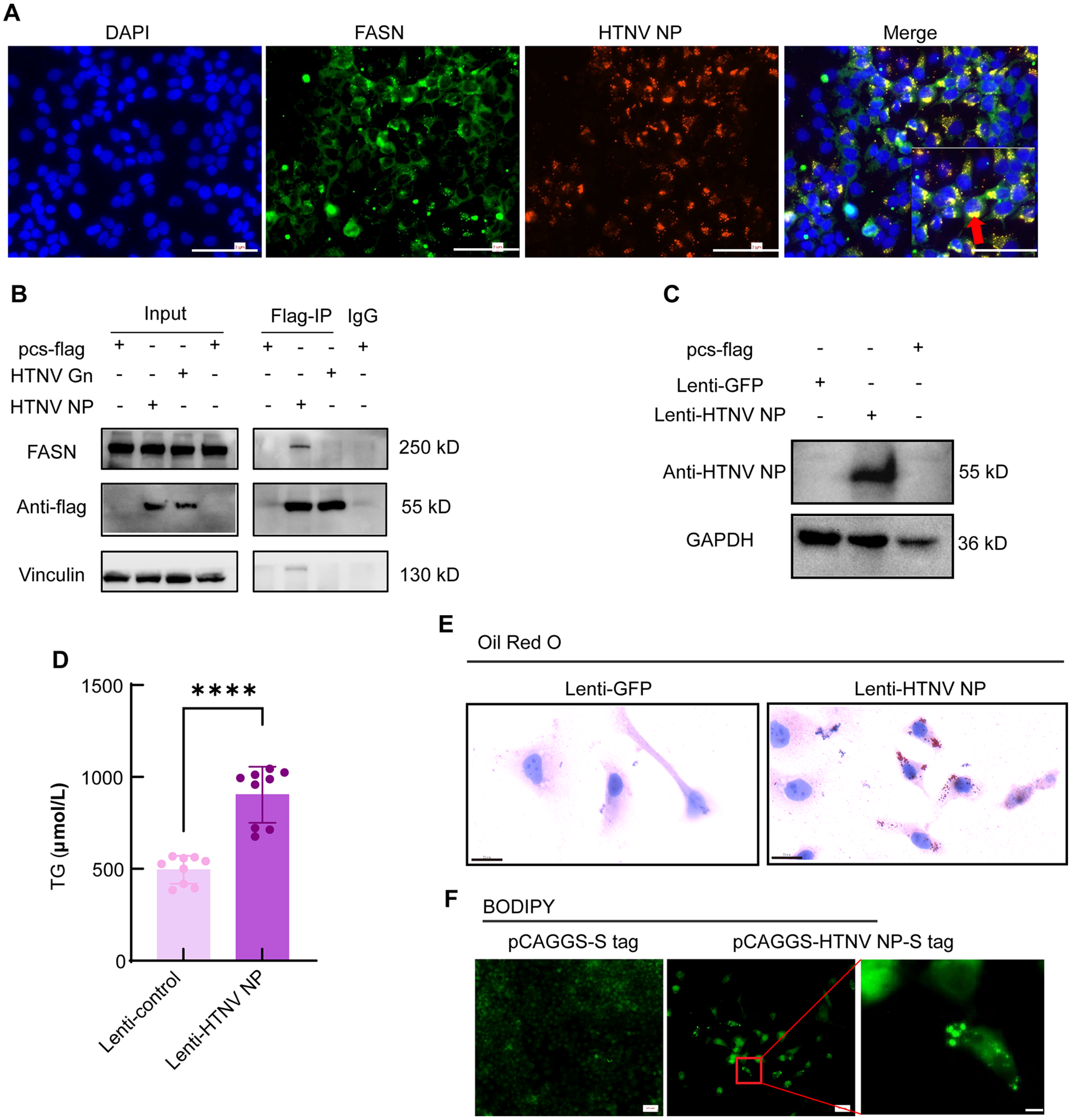

Figure 5 FASN interacts with HTNV NP

A: Immunofluorescence analysis showing colocalization of HTNV NP and FASN. HeLa cells were infected with HTNV at an MOI of 0.5, followed by fixation and immunofluorescence staining using a mouse anti-FASN antibody and a rabbit anti-HTNV NP antibody. Scale bar: 2 μm for the left panel and 500 nm for the magnified view of boxed areas on the right. B: Co-immunoprecipitation analysis of the interaction between HTNV NP and FASN. Cells were transfected with PCS2-Flag, pTomo-HTNV S-ORF-Flag-P2A-HygR, or PCS2-HTNV Gn-Flag plasmids. After 48 h, cell lysates were collected for analysis of PCS2-HTNV NP-Flag, PCS2-HTNV Gn-Flag, and FASN expression. Remaining lysates were subjected to immunoprecipitation using anti-Flag antibody, followed by western blot analysis using rabbit anti-Flag antibody or mouse anti-FASN antibody. Vinculin was used as a loading control. C: Western blot analysis of HTNV NP expression in HeLa cells. HeLa cells were infected with lenti-HTNV NP and subjected to antibiotic selection for 48 h. HTNV NP expression was detected with rabbit anti-HTNV NP antibody. HeLa cells infected with lenti-GFP served as controls. Vinculin was used as a loading control. D: Effect of HTNV NP on intracellular TG levels. HeLa cells infected with lenti-HTNV NP were subjected to antibiotic selection for 48 h, then reinfected with HTNV at an MOI of 0.5. Cellular TG content was measured. HeLa cells infected with lenti-GFP served as controls. Data are presented as mean±SD. ***: *P*<0.0001. Statistical significance was determined using Student's *t*-test. E, F: Effect of HTNV NP expression on lipid droplet accumulation in HeLa cells. HeLa cells infected with lenti-HTNV NP lentivirus were subjected to antibiotic selection for 48 h, then reinfected with HTNV at an MOI of 0.5. Lipid droplets were visualized by Oil Red O staining. HeLa cells infected with lenti-GFP lentivirus served as controls (E). Scale bar: 25 μm. HeLa cells transfected with an HTNV NP expression plasmid were stained with BODIPY to detect lipid droplets. HeLa cells transfected with empty pCAGGS vector served as controls (F). Scale bar: 50 μm for the left panel and 10 μm for the magnified view of boxed areas on the right.

substrate for protein palmitoylation, a reversible lipid modification required for membrane anchoring and functional regulation of many viral and host proteins (Loperena González et al., 2025). Comparable FASN-dependent palmitoylation has been implicated in the life cycle of influenza A virus (Veit et al., 2013), HCV (Huang et al., 2013), and SARS-CoV-2 (Tanner & Alfieri, 2021), raising the possibility that HTNV NP or additional structural proteins may undergo analogous lipid modification to support efficient viral assembly and egress. More specifically, interaction between NP and FASN was associated with redistribution and aggregation of FASN, a pattern that may concentrate fatty acid synthetic activity at subcellular sites associated with viral replication or budding and thereby promote lipid droplet biogenesis and other lipid-dependent steps in the infectious cycle. In parallel, both pharmacological inhibition and genetic knockdown of FASN enhanced expression of IFN-α, IFN-β, and ISGs in HTNV-infected cells (Supplementary Figure S4). These findings suggest that active lipogenesis may restrain antiviral signaling, consistent with recent evidence that FASN inhibition can potentiate RIG-I/MAVS signaling and restore IFN responses suppressed during viral infection (Liu et al., 2024; Loperena González et al., 2025).

Taken together, these results support a dual role for FASN during HTNV infection, functioning as both a metabolic facilitator of viral replication and a negative regulator of antiviral immunity. Initial *in vivo* evaluation in C57BL/6J mice showed that TVB-3664 did not measurably suppress TG synthesis or reduce viral loads across tissues, suggesting limited FASN inhibitory activity under the tested conditions. Further assessment of alternative FASN inhibitors is therefore also needed to determine whether pharmacological targeting of this pathway can be developed as an effective *in vivo* antiviral strategy against HTNV infection.

In conclusion, the tree shrew model established herein offers a physiologically relevant platform for investigating HTNV-host interactions. Our study identifies a previously underappreciated connection between lipid metabolic regulation and hantavirus pathogenesis centered on interaction between FASN and NP. Together, these insights provide a conceptual framework for host-directed antiviral strategies and establish the tree shrew as a valuable *in vivo* model for studying metabolic regulation of viral infections.

DATA AVAILABILITY

The raw RNA-sequencing data reported in this study have been deposited in the National Genomics Data Center (NGDC, https://ngdc.cncb.ac.cn/) under accession code PRJCA054252. All other data generated during the current study are included in the article.

SUPPLEMENTARY DATA

Supplementary data to this article can be found online.

COMPETING INTERESTS

The authors declare that they have no competing interests.

AUTHORS' CONTRIBUTIONS

Y.C.W.: Conceptualization, methodology, visualization, writing-original draft, Writing - Review & Editing; H.S.Q.: Data curation, validation, investigation; F.Y.L.: Data curation, format analysis; J.X.Y.: Data curation, validation, investigation; L.X.: Project administration; X.Q.G.: Resources; G.J.C.: Project administration; J.M.Z.: Conceptualization, writing-Review & Editing, funding acquisition; Y.G.Y.: Conceptualization, writing-Review & Editing, funding acquisition; X.L.Y.: Conceptualization, supervision, writing-Review & Editing, funding acquisition. All authors read and approved the final version of the manuscript.

ACKNOWLEDGMENTS

We thank the technical support from the Animal Center, the BSL-3 Laboratory, and the Large Facilities Center of the Kunming Institute of Zoology.

REFERENCES

Bolger AM, Lohse M, Usadel B. 2014. Trimmomatic: a flexible trimmer for Illumina sequence data. *Bioinformatics*, **30**(15): 2114–2120.

Dang YM, Wang Y, Wei J, et al. 2024. 25-Hydroxycholesterol inhibits Hantavirus infection by reprogramming cholesterol metabolism. *Free Radical Biology and Medicine*, **224**: 232–245.

Dias SSG, Soares VC, Ferreira AC, et al. 2020. Lipid droplets fuel SARS-CoV-2 replication and production of inflammatory mediators. *PLoS Pathogens*, **16**(12): e1009127.

Feng Y, Feng YM, Lu CX, et al. 2017. Tree shrew, a potential animal model for hepatitis C, supports the infection and replication of HCV *in vitro* and *in vivo*. *Journal of General Virology*, **98**(8): 2069–2078.

Guo J, Guo XL, Wang Y, et al. 2017. Cytokine response to *Hantaan virus* infection in patients with hemorrhagic fever with renal syndrome. *Journal of Medical Virology*, **89**(7): 1139–1145.

Heaton NS, Randall G. 2011. Multifaceted roles for lipids in viral infection. *Trends in Microbiology*, **19**(7): 368–375.

Huang JT, Tseng CP, Liao MH, et al. 2013. Hepatitis C virus replication is modulated by the interaction of nonstructural protein NS5B and fatty acid synthase. *Journal of Virology*, **87**(9): 4994–5004.

Jeyachandran AV, Irudayam JI, Dubey S, et al. 2025. Differential tropisms of old and new world hantaviruses influence virulence and developing host-directed antiviral candidates. *PLoS Pathogens*, **21**(8): e1013401.

Jonsson CB, Figueiredo LTM, Vapalahti O. 2010. A global perspective on hantavirus ecology, epidemiology, and disease. *Clinical Microbiology Reviews*, **23**(2): 412–441.

Khaiboullina SF, Rizvanov AA, Deyde VM, et al. 2005. Andes virus stimulates interferon-inducible MxA protein expression in endothelial cells. *Journal of Medical Virology*, **75**(2): 267–275.

Kim D, Paggi JM, Park C, et al. 2019. Graph-based genome alignment and genotyping with HISAT2 and HISAT-genotype. *Nature Biotechnology*, **37**(8): 907–915.

Li ML, Tian WW, Gao YD, et al. 2012. Genome-wide prediction of interferon family members of tree shrew and their molecular characteristics analysis. *Zoological Research*, **33**(1): 67–74. (in Chinese)

Liao Y, Smyth GK, Shi W. 2014. featureCounts: an efficient general purpose program for assigning sequence reads to genomic features. *Bioinformatics*, **30**(7): 923–930.

Liu RR, Ma RX, Liu ZY, et al. 2021a. HTNV infection of CD8$^+$ T cells is associated with disease progression in HFRS patients. *Communications Biology*, **4**(1): 652.

Liu SS, Bai TT, Que TL, et al. 2024. PI3K/AKT mediated De novo fatty acid synthesis regulates RIG-1/MDA-5-dependent type I IFN responses in BVDV-infected CD8$^+$T cells. *Veterinary Microbiology*, **291**: 110034.

Liu YY, Liang XD, Liu CC, et al. 2021b. Fatty acid synthase is involved in classical swine fever virus replication by interaction with NS4B. *Journal of Virology*, **95**(17): e0078121.

Loperena González PN, Karthigeyan KP, Corry J, et al. 2025. Mammalian fatty acid synthase: a commonly used viral host dependency factor and a putative target for host-targeted broad-spectrum antiviral therapeutic development. *mBio*, **16**(8): e03954–24.

Majdoul S, Compton AA. 2022. Lessons in self-defence: inhibition of virus entry by intrinsic immunity. *Nature Reviews Immunology*, **22**(6): 339–352.

McElroy AK, Bray M, Reed DS, et al. 2002. Andes virus infection of cynomolgus macaques. *The Journal of Infectious Diseases*, **186**(12): 1706–1712.

McKee KT, Jr., Kim GR, Green DE, et al. 1985. Hantaan virus infection in suckling mice: virologic and pathologic correlates. *Journal of Medical Virology*, **17**(2): 107–117.

Menendez JA, Lupu R. 2007. Fatty acid synthase and the lipogenic phenotype in cancer pathogenesis. *Nature Reviews Cancer*, **7**(10): 763–777.

Mittler E, Dieterle ME, Kleinfelter LM, et al. 2019. Hantavirus entry: perspectives and recent advances. *Advances in Virus Research*, **104**: 185–224.

Ohol YM, Wang ZT, Kemble G, et al. 2015. Direct inhibition of cellular fatty acid synthase impairs replication of respiratory syncytial virus and other respiratory viruses. *PLoS One*, **10**(12): e0144648.

Reddy SP, Narang KK, Patil SR. 2023. A very rare combination of hantavirus cardiopulmonary syndrome and hanta hemorrhagic fever with renal syndrome. *Journal of Global Infectious Diseases*, **15**(2): 88–89.

Robinson MD, McCarthy DJ, Smyth GK. 2010. edgeR: a Bioconductor package for differential expression analysis of digital gene expression data. *Bioinformatics*, **26**(1): 139–140.

Sanada T, Yasui F, Honda T, et al. 2019. Avian H5N1 influenza virus infection causes severe pneumonia in the Northern tree shrew (*Tupaia belangeri*). *Virology*, **529**: 101–110.

Sehgal A, Mehta S, Sahay K, et al. 2023. Hemorrhagic fever with renal syndrome in Asia: history, pathogenesis, diagnosis, treatment, and prevention. *Viruses*, **15**(2): 561.

Tang WC, Lin RJ, Liao CL, et al. 2014. Rab18 facilitates dengue virus infection by targeting fatty acid synthase to sites of viral replication. *Journal of Virology*, **88**(12): 6793–6804.

Tanner JE, Alfieri C. 2021. The fatty acid lipid metabolism nexus in COVID-19. *Viruses*, **13**(1): 90.

Terajima M, Ennis FA. 2011. T cells and pathogenesis of hantavirus cardiopulmonary syndrome and hemorrhagic fever with renal syndrome. *Viruses*, **3**(7): 1059–1073.

Tsui Y, Wu XQ, Zhang X, et al. 2025. Short-chain fatty acids in viral infection: the underlying mechanisms, opportunities, and challenges. *Trends in Microbiology*, **33**(3): 302–320.

Vaheri A, Strandin T, Hepojoki J, et al. 2013. Uncovering the mysteries of hantavirus infections. *Nature Reviews Microbiology*, **11**(8): 539–550.

Veit M, Serebryakova MV, Kordyukova LV. 2013. Palmitoylation of influenza virus proteins. *Biochemical Society Transactions*, **41**(1): 50–55.

Vial PA, Ferrés M, Vial C, et al. 2023. Hantavirus in humans: a review of clinical aspects and management. *The Lancet Infectious Diseases*, **23**(9): e371–e382.

Vogt DA, Camus G, Herker E, et al. 2013. Lipid droplet-binding protein TIP47 regulates hepatitis C Virus RNA replication through interaction with the viral NS5A protein. *PLoS Pathogens*, **9**(4): e1003302.

Wakil SJ, Abu-Elheiga LA. 2009. Fatty acid metabolism: target for metabolic syndrome. *Journal of Lipid Research*, **50**(S1): S138–S143.

Wang PZ, Li ZD, Yu HT, et al. 2012. Elevated serum concentrations of inflammatory cytokines and chemokines in patients with haemorrhagic fever with renal syndrome. *Journal of International Medical Research*, **40**(2): 648–656.

WHO. 2024. Pathogens prioritization: a scientific framework for epidemic and pandemic research preparedness. https://www.who.int/publications/m/item/pathogens-prioritization-a-scientific-framework-for-epidemic-and-pandemic-research-preparedness.

Wu TZ, Hu EQ, Xu SB, et al. 2021. clusterProfiler 4.0: a universal enrichment tool for interpreting omics data. *The Innovation*, **2**(3): 100141.

Wu WY, Chen RL, Wan YD, et al. 2022. Acetyl-CoA carboxylase (ACC) inhibitor, CP640186, effectively inhibited dengue virus (DENV) infection via regulating ACC phosphorylation. *Molecules*, **27**(23): 8583.

Xu L, Yu DD, Ma YH, et al. 2020. COVID-19-like symptoms observed in Chinese tree shrews infected with SARS-CoV-2. *Zoological Research*, **41**(5): 517–526.

Yamanouchi T, Domae K, Tanishita O, et al. 1984. Experimental infection in newborn mice and rats by hemorrhagic fever with renal syndrome (HFRS) virus. *Microbiology and Immunology*, **28**(12): 1345–1353.

Yang C, Ruan P, Ou C, et al. 2015. Chronic hepatitis B virus infection and occurrence of hepatocellular carcinoma in tree shrews (*Tupaia belangeri chinensis*). *Virology Journal*, **12**(1): 26.

Yang JX, Luo EE, Wu YC, et al. 2025. Phloroglucinol oligomers from *Callistemon rigidus* as novel anti-hantavirus replication agents. *Viruses*, **17**(7): 916.

Yao YG, Lu L, Ni RJ, et al. 2024. Study of tree shrew biology and models: a booming and prosperous field for biomedical research. *Zoological Research*, **45**(4): 877–909.

Ye MS, Zhang JY, Yu DD, et al. 2021. Comprehensive annotation of the Chinese tree shrew genome by large-scale RNA sequencing and long-read isoform sequencing. *Zoological Research*, **42**(6): 692–709.

Yoshimatsu K, Arikawa J, Ohbora S, et al. 1997. Hantavirus infection in SCID mice. *Journal of Veterinary Medical Science*, **59**(10): 863–868.

Yu DD, Kang WB, Ma YH, et al. 2026. Single-cell atlas of hepatitis C virus inoculated tree shrew liver reveals immune activation, metabolic reprogramming, and persistent inflammation. *eBioMedicine*, **123**: 106080.

Yu GC, Wang LG, Han YY, et al. 2012. clusterProfiler: an R package for comparing biological themes among gene clusters. *OMICS: A Journal of Integrative Biology*, **16**(5): 284–287.

Yuan SF, Chu H, Chan JFW, et al. 2019. SREBP-dependent lipidomic reprogramming as a broad-spectrum antiviral target. *Nature Communications*, **10**(1): 120.

Zhao Y, Wang JB, Kuang DX, et al. 2020. Susceptibility of tree shrew to SARS-CoV-2 infection. *Scientific Reports*, **10**(1): 16007.